Quantifying chiral handedness of core-shell inorganic nanotube photocatalysts via electron microscopy and diffraction

Kaiyuan Wang,[a] *Beilynn Geiss,*[b] *Roy Geiss,*[c] *James R. Neilson,*[a] *Alla Zak,*[d] *Justin B. Sambur*[a]

[a]Department of Chemistry, Colorado State University, 200 West Lake Street, Fort Collins, Colorado 80523-1872, United States.

[b]Skidmore College, Saratoga Springs, New York 12866, United States.

[c]Analytical Resources Core, Colorado State University, 200 West Lake Street, Fort Collins, Colorado 80523-1872, United States.

[d] Faculty of Science, Holon Institute of Technology, Holon 5810201, Israel.

KEYWORDS. Inorganic nanotubes, chirality, single particle imaging, TEM, nanostructures

Abstract

Intrinsically chiral inorganic nanotubes (NTs) based on WS_2 and MoS_2 are promising visible-light-absorbing materials for heterogeneous enantioselective photocatalysis and, potentially, for fundamental studies of the chiral induced spin selectivity (CISS) effect. Accurate identification of chiral handedness is essential for advancing enantioselective applications of these materials, but existing imaging and diffraction-based protocols do not rapidly facilitate the identification of NT handedness. We present a combined transmission electron microscopy (TEM) and selected-area electron diffraction (SAED) approach for determining the chiral handedness of WS_2 NTs that contain WO_x cores. We observe the WO_x core lattice and WS_2 atomic layers in the same TEM image. By comparing the lattice orientations of the WO_x core relative to the WS_2 layers, and confirming that relationship with the chiral angle revealed by SAED patterns, we can unambiguously identify the right- or left-handed structure of individual NTs. In addition, we show that moiré patterns formed from the WS_2 shells and oxide core can also be used to characterize lattice orientation, chiral indices, and handedness. This approach requires no additional sample preparation, instrumentation, or experimental adjustments, and may be applied broadly to other core-shell nanotube systems such as MoS_2, BN, and carbon NTs. The significance of this work is that it enables reliable handedness determination of chiral core-shell nanostructures and addresses a key difficulty in the existing characterization methods of multiwalled NTs. We envision that the single particle catalysis community can leverage these methods to study structure-activity relationships of this unique class of intrinsically chiral semiconductor nanostructures.

Introduction

Inorganic NTs are exciting materials that have been explored for applications in lubricants,[1] superconductor,[2] battery,[3] photocatalysts,[4,5] and hydrogen storage.[6,7] NTs based on transition metal dichalcogenides (TMDs) such as MoS_2 and WS_2 are emerging as intriguing materials due to their inherently chiral surfaces[8,9], which opens possibilities for a broad range of applications spanning spin-selective catalysis[10–13], chiral molecule sensing[14], and light–matter interactions.[15]

The central challenge in advancing inorganic NTs for enantioselective chemical synthesis applications is that current synthesis methods produce racemic mixtures with wide variations in diameter, wall thickness, chiral index, and handedness. WS_2 NTs grow from $W_{18}O_{49}$ nanowhiskers.[16–18] The high-temperature sulfurization of the $W_{18}O_{49}$ nanowhiskers yields an oxide core sheathed by a few closed layers of WS_2.[19] This process leads to a core-shell $W_{18}O_{49}$@WS_2 nanostructure, and the NT diameter and chirality depends on the heterogeneous size distribution of $W_{18}O_{49}$ nanowhiskers. This structural heterogeneity makes it difficult to connect structure with function using conventional ensemble-averaged characterization tools. Moreover, oxide cores can influence catalysis[20] and may facilitate photogenerated charge-carrier separation at the core–shell interface, yet there are no established methods for characterizing the chiral structural properties of these core–shell architectures at the single-nanotube level, particularly the chiral handedness of each INT in the heterogeneous sample batch.

Several characterization approaches have been used to determine the chiral structural properties of single and double-walled carbon NTs, each with advantages and disadvantages. Electron diffraction is the most widely used approach to determine the chiral indices of carbon NTs,[21,22] but this approach does not directly reveal the chiral handedness (i.e., right- or left-handed NT). Liu and Qin proposed a method using the principal line shift in the SAED pattern to determine the handedness of carbon NTs.[23] However, this approach relies on applying a mechanical force to twist an individual NT and then use changes in the SAED pattern to distinguish between left- and right-handed structures, which is challenging to implement experimentally. Atomic force microscopy (AFM) and scanning tunneling microscopy (STM) can determine the helical angle and handedness of single-wall carbon NTs.[24,25] However, scanning probe methods can only detect a nanoscale region of the outermost surface layer and are not sensitive to the chirality of multi-wall NTs. Practically, AFM and STM measurements are difficult to perform over large areas and for curved surfaces.[26] Liu et al. developed a Rayleigh scattering circular dichroism technique that can characterize the chiral indices and handedness of a single-wall carbon NT.[27] This all-optical approach effectively amplifies weak chiroptical signal by nearly four orders of magnitude, but it requires specialized optical expertise, hardware, and additional sample preparation that suspends a single NT across a micrometer scale slit.

Atomic-resolution TEM imaging has also been employed to determine the chiral handedness of single and double-walled carbon NTs.[28] Liu, et al., determined the handedness of double-wall carbon NTs[29] by carefully tilting the NT sample relative to the electron beam, revealing asymmetric lattice fringes that facilitate chirality determination. However, this approach demands that the NT must also be oriented nearly perpendicular to the tilt axes to avoid misassignment. Also, the tilting approach is only reliable for few-walled NTs because multiple walls cause severe fringe overlap. Yu, et al., developed a method that aligned single-wall carbon NTs with a graphene substrate and used TEM to determine handedness.[30] However, this approach requires depositing samples on a graphene substrate, which can be difficult to fabricate and may not suit all applications where correlated studies on other substrates are preferred.

Before presenting our approach and results, we first illustrate the characterization challenge by reviewing how chiral NT structures are defined and visualized in a TEM. Figure 1 illustrates how chiral WS_2 nanotubes (NTs) form from 2D sheets and why their handedness is challenging to determine by TEM alone. In Figure 1a (top), the hexagonal WS_2 lattice is shown "rolled" along the red arrow between dashed lines, producing a left-handed NT with chiral indices (m,n) = (3, 9). Figure 1b then presents an edge on view of the resulting NT, divided into two segments: the upper portion above the black line in Figure 1band the lower portion below it. The projection of these two segments generates the moiré pattern observed in TEM imaging (Figure 1e). Figure 1f-g shows the analogous process for a right-handed NT with indices (m,n) = (9, 3). Here, the relative positions of the upper and lower portions are interchanged, yet the projected TEM images yield the same moiré pattern.[30] The presence of the moiré patterns in our samples was validated by high-angle annular dark-field scanning transmission electron microscopy (HAADF-STEM) imaging (Figure S1). The key point is that enantiomeric NTs produce indistinguishable 2D projections. Consequently, the absence of a rapid and reliable method for handedness identification has significantly hindered the use of WS_2 NTs in chiral applications.

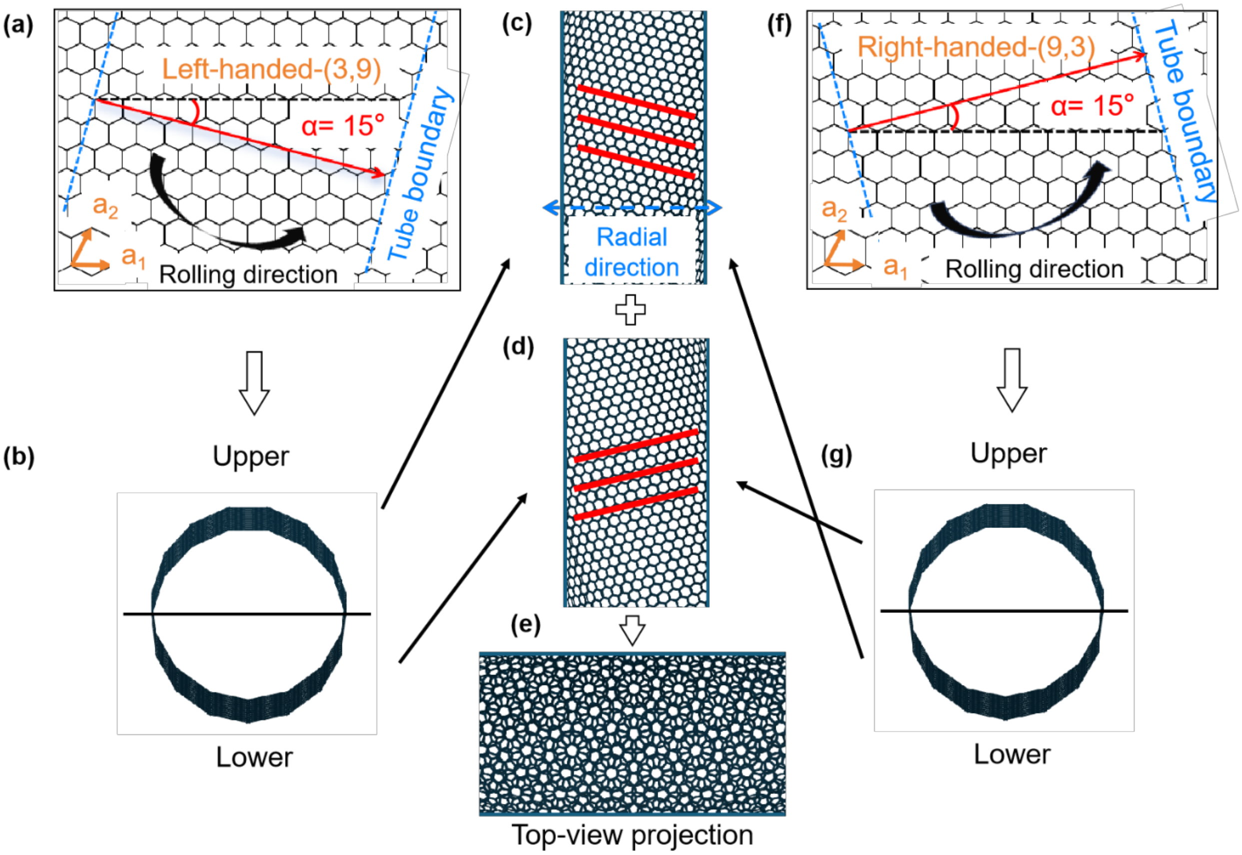

Figure 1. Cartoon illustration showing how WS_2 NTs form from two-dimensional sheets, how sheets roll to form a NT, and how the upper and lower portions of a NT appear in a top-down image such as in a TEM image. **(a)** Top-down view of a hexagonal lattice where the blue lines indicate the NT edges, the dashed black line represents the a_1 lattice direction, the red arrow represents the lattice vector formed from the chiral indices (m,n) = (3, 9). The chiral angle $\alpha = 15°$ is defined as the angle between the dashed black line and the chiral vector. A chiral NT forms upon rolling the two-dimensional sheet from left to right along the lattice vector (as indicated by the arrow in panel a). **(b)** Edge-on view of the NT that forms upon rolling the lattice in panel a. The solid black line represents a dividing line between the top and bottom portions of the NT. **(c, d)** Top-down views of the top and bottom portions of the NT in panel b, respectively. **(e)** Top-down view of the moiré pattern that forms from a combination of the top and bottom portions in panels

(c and d). **(f and g)** are the same as panels (a and b), but for a right-handed NT with (m,n) = (9,3) with the same chiral angle (15°). In this case, the top portion of the NT corresponds to panel d and the bottom portion corresponds to panel c. Both NTs produce the same moiré pattern. Importantly, both NTs produce the same moiré pattern.

Another major challenge in determining NT handedness arises from the gap between its formal definition and how samples are viewed and characterized. By definition, right-handed NTs exhibit chiral angles between 0–30°, while left-handed NTs fall between 30–60°.[24,31] This definition, however, assumes that the observer views the NT from a fixed reference orientation. In practice, NTs deposited on substrates may appear rotated, flipped, or inverted, making it unclear whether we are viewing a right- or left-handed NT. The situation is analogous to looking at human hands: a right hand is easily distinguished from a left hand in person, but in a photograph or mirror image the distinction may become ambiguous.

In this work, we developed an approach to unambiguously identify the handedness of chiral core–shell WO_x–WS_2 NTs using TEM imaging and selected area electron diffraction (SAED). The oxide core provides a strong lattice contrast that serves as a built-in reference frame for chiral handedness determination. Importantly, this strategy requires no additional sample preparation. We further show that TEM imaging and SAED yield consistent chiral angles in real and reciprocal space. By overcoming a key bottleneck in handedness determination, this advance lays the foundation for employing WS_2 NTs in fundamental studies of heterogeneous enantioselective photocatalysis and other emerging applications.

Results and Discussions

Figure 2a shows a top-down TEM image and Figure 2b shows an edge-on TEM image of an individual multi-walled WS_2 NT surrounding a tungsten oxide-based core. The red lines in Figure 2a indicates the presence of eight continuous WS_2 layers. A distinct contrast variation appears at the core/shell interface. The oxide core exhibits a periodic stripe-like lattice, indicating the oxide core is crystalline (Figure 2a-inset). The NT appearance in Figure 2a suggests a cylindrical morphology, however the NT exhibits a prismatic cross-section with polygonal faces (Figure 2b). For this reason, the WS_2 layers on the right and left sides of the NT in Figure 2a do not produce similar contrast in TEM images.

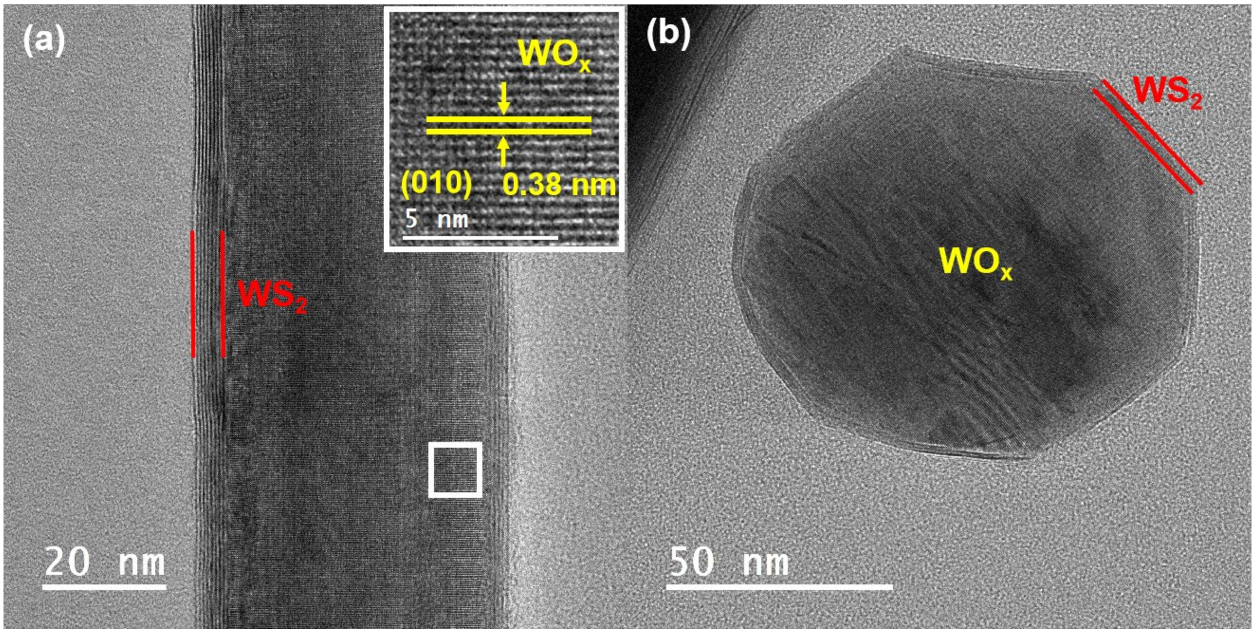

Figure 2. **(a)** TEM image of an eight-layer-thick core-shell WO_x-WS_2 NT viewed along the longitudinal axis. The inset shows a zoomed-in view of the oxide/shell interface indicated by the white box. The yellow lines display the (010) lattice spacing of 0.37Å. **(b)** TEM image of a different four-layer core-shell WO_x-WS_2 NT viewed along the axial axis. The red lines indicate the WS_2 lattice orientation.

Despite the oxide core dominating the TEM contrast (white box, Figure 2a), lattice fringes from the upper WS_2 layers remain clearly visible in many high-resolution TEM images. Figure 3 shows representative images where lattice fringes from both WS_2 and WO_x are clearly visible. The lattice fringes of WS_2 likely stem from the upper WS_2 layers because any contribution from the lower WS_2 layers are strongly attenuated by the oxide core (see Figure 1c-d for an illustration of the top and bottom NT views and TEM projections). As the electron beam enters the nanotube from the top, the upper WS_2 layers are the first region where the electron wave can interact coherently with the atoms in the material, generating lattice-fringe phase contrast. After propagating through the thick oxide core, strong inelastic scattering associated with the high atomic number of tungsten is expected to reduce the coherence of the electron wave, thereby attenuating any lattice-fringe contribution from the lower WS_2 layers. We developed a step-by-step procedure, described and illustrated in Figure S2 and Figure S3 of the Supplementary Information, to confirm that the lattice fringes in Figure 3 stem from the WS_2 layers. Briefly, the procedure consists of generating an FFT from a selected area of the TEM image, selecting the FFT spots associated with the WS_2 lattice, and applying an inverse FFT to those spots alone to reconstruct a real-space image that reveals the WS_2 lattice-fringe orientation.

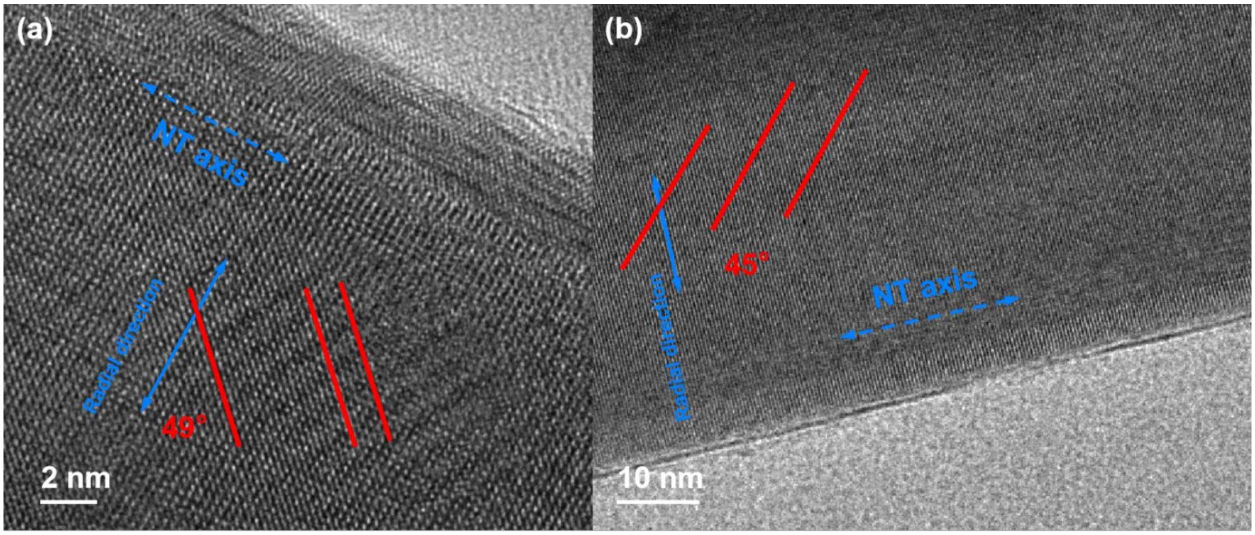

Figure 3. TEM images of WO_x/WS_2 NTs where the WS_2 lattice fringes are oriented **(a)** 49° and **(b)** 45° relative to the radial direction of the NT (blue lines).

Before we introduce our approach to determine handedness of INTs using real space TEM imaging, we briefly review how to determine the chiral angle of a single NT using SAED. Figure 4 schematically shows the SAED analysis procedure for a 3-layer thick chiral WS_2 NT. The chiral angles from SAED patterns are calculated using $D_1=D_2+D_3$,[31] where D_1, D_2, and D_3 represent the distances between the equatorial line and the first, second, and third diffraction lines of WS_2, respectively (from top toward the equatorial line). The equatorial line corresponds to the diffraction from lattice planes that are perpendicular to the NT axis. Each WS_2 layer produces a diffraction line and, therefore, the number of diffraction lines correlates to the number of WS_2 layers. In Figure 4, a three layer-thick NT produces diffraction features (arising from the hexagonal lattice) composed of three streaks. These streaks correspond to diffraction from the three concentric layers of the NT wall. Within each set, the streak furthest from the center originates from the innermost layer with the smallest diameter, while the streak closest to the center arises from the outermost layer with the largest diameter.

The chiral angle α is calculated using:

$$\alpha = tan^{-1}(\frac{2D_2 - D_1}{\sqrt{3}\,D_1}) = tan^{-1}(\frac{D_1 - 2D_3}{\sqrt{3}\,D_1}) = tan^{-1}(\frac{D_2 - D_3}{\sqrt{3}\,(D_2 + D_3)})$$

All layers of a multilayer WS_2 NT typically share the same handedness, differing only by a few degrees, and the measured angles can be assigned to individual layers in sequence.[31,32] Therefore, the average angle is taken in the SAED pattern by using the midpoint of each diffraction line to represent the average angle of this NT, as described in Figure S4. Following the approach by Deniz and Qin who showed that each layer in a multiwall WS_2 NT adopts similar chiral structures,[32] we assume that each layer of a multiwalled NT shares the same handedness. The rationale for this assumption and the consequences of chiral angle averaging are discussed in the Discussion section.

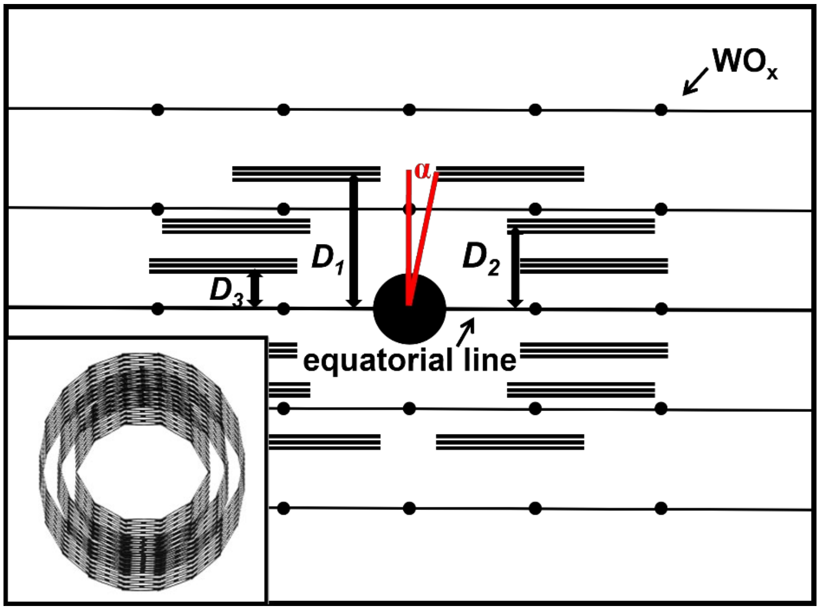

Figure 4. Cartoon illustration of an idealized SAED pattern of a three layer-thick chiral core-shell WO_x-WS_2 NT. D_1, D_2, and D_3 represent the distances between the equatorial line and the first, second, and third diffraction lines of WS_2, respectively (from top toward the equatorial line). The angle α indicates the chiral angle. The black dots represent WO_x reflections. The inset shows the corresponding simulated three-layer WS_2 NT structure.

Having discussed how to determine the chiral angle via SAED, we now show how the unique TEM image contrast produced by the upper WS_2 layers can be used to determine the right- or left-handedness of a single NT, which cannot be done for hollow WS_2 NTs. Figure 5a shows low- and high-resolution TEM images of a 2-layer thick WO_x-WS_2 NT. The critical angle observed via SAED is 16° (Figure 5a-top right inset). However, the SAED-derived angle does not reveal the chiral handedness directly. Figure 5b-c shows the possible lattice orientations for right- and left-handed NTs with 60° symmetry and the same SAED-derived chiral angle of 16°. Next, we compare the lattice fringes determined via TEM imaging (Figure 5a-bottom right inset) to the two possible configurations in Figure 5b-c. For this NT, we observe WS_2 lattice fringes oriented 46° relative to the NT radial direction, as indicated by the red lines in the bottom right inset of Figure 5a. The right-handed NT configuration shown in Figure 5b illustrates a right-handed chiral INT where the lattice orientation of the WS_2 lattice fringes would be oriented 44° relative to the NT radial direction, which is 2° less than the 46° angle measured in real space TEM images. The small 2° difference between the SAED- and TEM-derived angles (44° versus 46°, respectively) is likely due to the fact that it is difficult to determine which layer in the multi-layer wall structure contributes to the contrast in TEM imaging; SAED is, in principle, able to distinguish each chiral layer from each layer (see Figure 4). The key point of Figure 5a-c is that the 46° angle obtained from real-space imaging relates to the SAED-determined angle of 16° via 60° symmetry, revealing the handedness of a single NT.

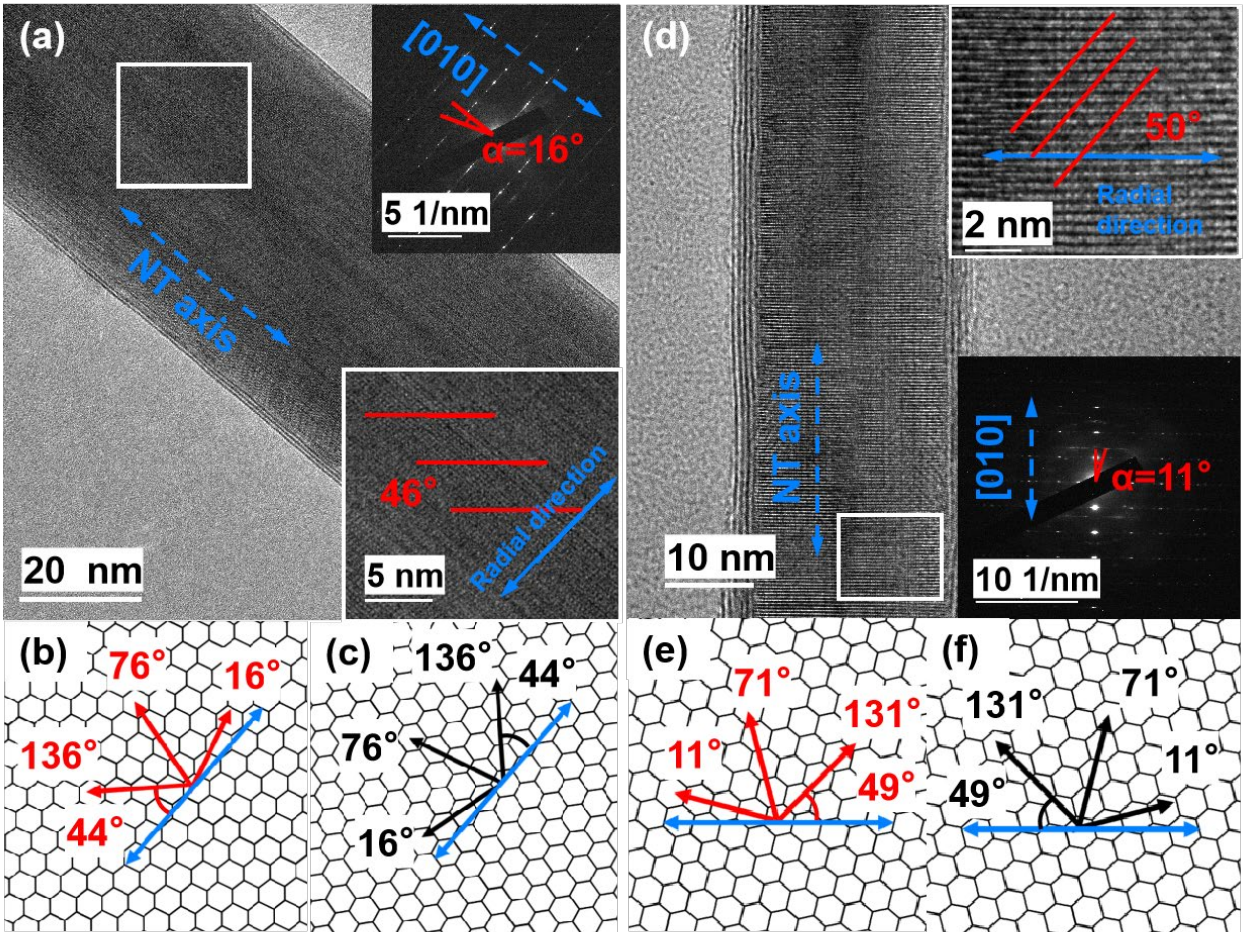

Figure 5. Two examples showing the consistency of chiral angles measured by TEM and SAED. **(a)** TEM image of a right-handed two-layer-thick WS_2 NT. The top right inset shows the SAED pattern and the chiral angle determined from SAED analysis. The bottom right inset shows a zoomed-in view from the white box region in panel a. The blue arrow indicates the radial direction of the NT and the red lines represent the WS_2 lattice. The [010] direction is displayed by a blue arrow in the SAED insert. **(b-c)** The reference frame of panel a that relates the right-handed (b, red) and left-handed (c, black) TEM-derived angle (46°) to the chiral angle measured via SAED (16°). **(d-f)** Same as panel a-c, but for a left-handed four-layer-thick WS_2 NT. In panels b-c and e-

f, red frames indicate the WS_2 lattice orientation corresponding to the correct handedness assignment, whereas black frames indicate the incorrect handedness for comparison.

Figure 5d-f further illustrates the consistency between real space TEM imaging and SAED for a left-handed, four-layer thick NT. In this case, the SAED-derived angle is 11° (Figure 5d-bottom right inset). Figure 5e-f shows two possible WS_2 lattice orientations with the chiral angle of 11°. High-resolution TEM imaging reveals a 50° angle between the WS_2 lattice and the radial NT direction (Figure 5d-top right inset). Following the symmetry argument discussed above, one can see how the SAED angle of 11° corresponds to a TEM-determined value of 50° for the left-handed configuration in Figure 5e. Another right-handed example is shown in Figure S5 and Figure S6.

In some cases, moiré patterns appear in TEM images of core-shell NTs and provide another direct and straightforward way to define the chiral handedness. Figure 6 shows NTs with moiré patterns that arise from the superposition of the WS_2 lattice and the WO_x core lattice. The stripe-like lattice of tungsten oxide readily produces moiré patterns. These stripe-like patterns are distinct from the WS_2 lattice. We distinguish the WO_x lattice from the WS_2 lattice by its alternating contrast and its larger periodic spacing compared to WS_2, as shown in Figure 6.

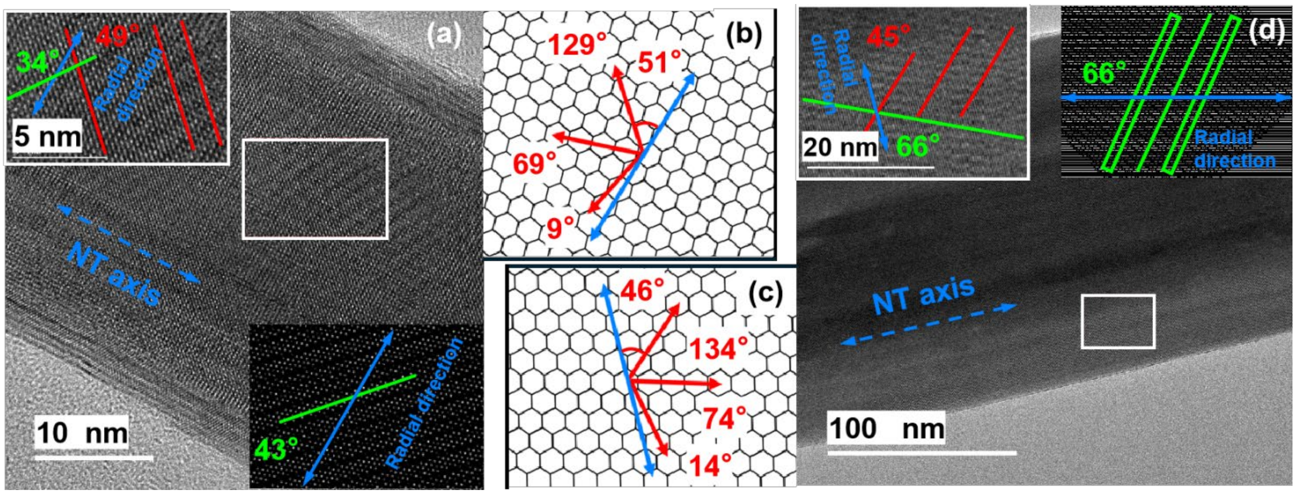

Figure 6. Utilizing moiré patterns for chiral handedness identification. **(a)** TEM image of a left-handed 5-layer multi-walled WS_2 NT with a visible stripe-like moiré pattern. Top left inset shows a zoomed-in view of the moiré pattern from the white boxed region in panel a. In the top left inset panel, the red and green lines represent the WS_2 lattice and moiré pattern, respectively. The 49° and 34° represent the angles formed by the WS_2 lattice and the moiré pattern relative to the radial direction, which is represented with a blue double-sided arrow. The bottom right inset shows the moiré pattern simulation. **(b)** Cartoon illustration of the reference frames depicting the chiral angles and relative orientation of the WS_2 lattice relative to the NT radial direction for the NTs in a. **(c-d)** Same as panel a-b, but for a right-handed single-walled WS_2 NT.

Figure 6a illustrates a representative case for determining chiral handedness using moiré patterns formed between the WO_x core and WS_2 layers. Figure 6a-top left inset shows a distinct moiré pattern with a 34° left-oriented relative to the NT radial direction, whereas the WS_2 lattice exhibits a 49° right orientation. SAED analyses yield an average chiral angle of 9° (Figure S7a), which can be rationalized using the reference frame in Figure 6b. Hence, the NT in Figure 6a is left-handed with an 11° chiral angle. Simulations of a 49° right-oriented WS_2 NT and a WO_x core in Figure 6a (bottom right inset) predicts the opposite orienting relationship between the moiré pattern and WS_2 lattice: the overlap between the hexagonal WS_2 lattice points and the WO_x rectangular points. The simulated moiré pattern exhibits a 43° angle relative to the radial direction (Figure 6a-inset). We note the inconsistency between the TEM-derived angle and that of the simulated moiré pattern; a small misalignment or space difference results in a large change in the moiré pattern angle.[33] It is also possible that the multiwall structure contributes to the error between the TEM-derived value and SAED,[34] as discussed above.

The single-walled NT in Figure 6d shows a 66° moiré pattern, but oriented in a different direction relative to the NT radial direction as in Figure 6a. A zoom-in view confirms the WS_2 lattice is oriented 45° relative to the NT radial. This corresponds to a 15° chiral angle, which can be rationalized using the reference frame in Figure 6c, closely matching the SAED-derived 14° angle (Figure S7b). The accompanying simulation in Figure 6d-inset shows a 45°-rotated WS_2 lattice superimposed on the line-like tungsten oxide lattice, producing a moiré pattern with a 66° angle, consistent with the TEM observations. In all cases, we observed good agreement (<2°) between TEM-derived and SAED-derived chiral angles (Table 1). The slight disagreement between TEM- and SAED-derived chiral angles is likely due to the manual image analysis procedure. There is a critical need to develop automated and robust image analysis procedures that leverage data and simulations to define the chiral angle and handedness, which is beyond the scope of this work. However, the close agreement between TEM and SAED values demonstrates the repeatability and reliability of the proposed method despite the fact that multi-shelled NTs inherently exhibit a few degrees of variation in chiral angles among each shell.[31] The methods proposed herein can be extended to other core-shell NT materials (MoS_2 NTs[2,35,36], BN NTs[37], and carbon NTs[38,39]), where the core material provides a reference frame contrast for the chiral shell material.

Table 1. Comparison of chiral angles determined by TEM and SAED, their differences, and corresponding handedness assignments for WS_2 NTs.

Number	Chiral angle (TEM)	Chiral angle (SAED)	Difference	Handedness
1	11°	9°	2°	Left
2	15°	14°	1°	Right
3	12°	14°	2°	Right

4	10°	11°	1°	Left
5	14°	16°	2°	Right

Conclusions

In summary, we established a rapid, straightforward TEM approach for determining the handedness of core–shell WO_x-WS_2 NTs. The method leverages the strong contrast of the WO_x core, which effectively masks the lower WS_2 layers, allowing the handedness of the exposed upper layers to be identified in real-space TEM projections. The results were validated using SAED analysis and structural simulation. In some cases, analysis of WO_x-WS_2 moiré patterns provides additional verification. This strategy requires no specialized sample preparation and is broadly accessible in any high-resolution TEM. Beyond core-shell WO_x-WS_2, the principle of disentangling overlapping structural signals can be extended to other chiral nanostructures, enabling more reliable handedness assignment and opening opportunities for chirality-dependent applications of inorganic nanotubes.

Methods

NT synthesis. Core-shell WO_x-WS_2 NTs were synthesized in a horizontal reactor by sulfurization of the $W_{18}O_{49}$ nanowhiskers, as described previously.[19]

TEM sample preparation and characterization. The NTs were dispersed in anhydrous ethanol (200 proof), sonicated for 30 seconds in a sonicator (VWR 97044-002), and 5 μl of the solution was drop-cast onto a carbon-coated Cu TEM grid. After drop-casting, the TEM grids were dried in air for 2 h before imaging. High-resolution TEM imaging and SAED experiments were conducted on a JEOL JEM-2100F electron microscope operated at 200 kV. Images were acquired with a Gatan Ultrascan CCD camera using an acquisition time of 1-6 s. Image and SAED diffraction data were processed using Digital Micrograph software (v3.61).

Author contributions

Kaiyuan Wang: Conceptualization, formal analysis, methodology, investigation, resources, data curation, validation, visualization, original draft writing, review and editing. **Beilynn Geiss**: formal analysis, investigation, validation, methodology, original draft writing, review and editing. **Roy Geiss**: methodology, data curation, formal analysis, investigation, validation, original draft writing, review and editing. **James R. Neilson**: supervision, formal analysis, review. **Alla Zak**: supervision, synthesis of nanotubes, formal analysis, review. **Justin B. Sambur**: conceptualization, methodology, data curation, original draft writing, review and editing, project administration, funding acquisition.

Conflicts of interest

There are no conflicts to declare.

Data availability

All data generated or analyzed in this study are included in this article and the supplementary information (SI).

Acknowledgements

This work was supported by the donors of ACS Petroleum Research Fund under New Directions Grant 66052-ND10 and the National Science Foundation (DMR-2046948). A.Z. acknowledges support from the Ministry of Innovation, Science & Technology grants # 0006701 and #0007244, Israel.

References

(1) Tenne, R.; Redlich, M. Recent Progress in the Research of Inorganic Fullerene-like Nanoparticles and Inorganic Nanotubes. *Chem. Soc. Rev.* **2010**, *39* (5), 1423–1434. https://doi.org/10.1039/B901466G.

(2) Qin, F.; Shi, W.; Ideue, T.; Yoshida, M.; Zak, A.; Tenne, R.; Kikitsu, T.; Inoue, D.; Hashizume, D.; Iwasa, Y. Superconductivity in a Chiral Nanotube. *Nat Commun* **2017**, *8* (1), 14465. https://doi.org/10.1038/ncomms14465.

(3) Dey, S.; Manjunath, K.; Zak, A.; Singh, G. WS_2 Nanotube-Embedded SiOC Fibermat Electrodes for Sodium-Ion Batteries. *ACS Omega* **2023**, *8* (11), 10126–10138. https://doi.org/10.1021/acsomega.2c07464.

(4) Lin, J.; Hu, Z.; Li, H.; Qu, J.; Zhang, M.; Liang, W.; Hu, S. Ultrathin Nanotubes of Bi_5O_7I with a Reduced Band Gap as a High-Performance Photocatalyst. *Inorg. Chem.* **2019**, *58* (15), 9833–9843. https://doi.org/10.1021/acs.inorgchem.9b00858.

(5) Pignié, M.-C.; Shcherbakov, V.; Charpentier, T.; Moskura, M.; Carteret, C.; Denisov, S.; Mostafavi, M.; Thill, A.; Le Caër, S. Confined Water Radiolysis in Aluminosilicate Nanotubes: The Importance of Charge Separation Effects. *Nanoscale* **2021**, *13* (5), 3092–3105. https://doi.org/10.1039/D0NR08948F.

(6) Laikhtman, A.; Michaelson, S.; Hoffman, A.; Kim, T. K.; Moon, H. R.; Zak, A. Using Hydrogen Activated by Microwave Plasma vs. Molecular Hydrogen for Hydrogen Storage in Tungsten Disulfide Inorganic Nanotubes. *Int. J. Hydrog. Energy* **2014**, *39* (18), 9837–9841. https://doi.org/10.1016/j.ijhydene.2014.02.033.

(7) Musfeldt, J. L.; Iwasa, Y.; Tenne, R. Nanotubes from Layered Transition Metal Dichalcogenides. *Physics Today* **2020**, *73* (8), 42–48. https://doi.org/10.1063/PT.3.4547.

(8) Wilson, M. The Formation of Low-Dimensional Chiral Inorganic Nanotubes by Filling Single-Walled Carbon Nanotubes. *Chem. Phys. Lett* **2004**, *397* (4–6), 340–343. https://doi.org/10.1016/j.cplett.2004.08.036.

(9) Kachtík, L.; Citterberg, D.; Bukvišová, K.; Kejík, L.; Ligmajer, F.; Kovařík, M.; Musálek, T.; Krishnappa, M.; Šikola, T.; Kolíbal, M. Chiral Nanoparticle Chains on Inorganic Nanotube Templates. *Nano Lett.* **2023**, *23* (13), 6010–6017. https://doi.org/10.1021/acs.nanolett.3c01213.

(10) Yan, Y.; Shaikh, M.; Beard, M. C.; Gu, J.; Hendrix, I. Highly Enantioselective Synthesis Controlled by Spin-Exchange Interaction. *Sci. Adv* **2025**.

(11) Sang, Y.; Tassinari, F.; Santra, K.; Zhang, W.; Fontanesi, C.; Bloom, B. P.; Waldeck, D. H.; Fransson, J.; Naaman, R. Chirality Enhances Oxygen Reduction. *Proc. Natl. Acad. Sci. U.S.A.* **2022**, *119* (30), e2202650119. https://doi.org/10.1073/pnas.2202650119.

(12) Bloom, B. P.; Lu, Y.; Metzger, T.; Yochelis, S.; Paltiel, Y.; Fontanesi, C.; Mishra, S.; Tassinari, F.; Naaman, R.; Waldeck, D. H. Asymmetric Reactions Induced by Electron Spin Polarization. *Phys. Chem. Chem. Phys.* **2020**, *22* (38), 21570–21582. https://doi.org/10.1039/D0CP03129A.

(13) Metzger, T. S.; Mishra, S.; Bloom, B. P.; Goren, N.; Neubauer, A.; Shmul, G.; Wei, J.; Yochelis, S.; Tassinari, F.; Fontanesi, C.; Waldeck, D. H.; Paltiel, Y.; Naaman, R. The Electron Spin as a Chiral Reagent. *Angew Chem Int Ed* **2020**, *59* (4), 1653–1658. https://doi.org/10.1002/anie.201911400.

(14) Foo, Y. X.; Kermiche, A.; Chowdhury, F. T.; Aiello, C. D.; Smith, L. D. Mind the Gap: From Resolving Theoretical Foundations of Chiral(Ity)-Induced Spin Selectivity to Pioneering Implementations in Quantum Sensing. *Chemical Physics Reviews* **2025**, *6* (3), 031306. https://doi.org/10.1063/5.0244306.

(15) Dong, Y.; Hautzinger, M. P.; Haque, M. A.; Beard, M. C. Chirality-Induced Spin Selectivity in Hybrid Organic-Inorganic Perovskite Semiconductors. *Annu. Rev. Phys. Chem* **2025**, *76* (1), 519–537. https://doi.org/10.1146/annurev-physchem-082423-032933.

(16) Chithaiah, P.; Ghosh, S.; Idelevich, A.; Rovinsky, L.; Livneh, T.; Zak, A. Solving the "MoS2 Nanotubes" Synthetic Enigma and Elucidating the Route for Their Catalyst-Free and Scalable Production. *ACS Nano* **2020**, *14* (3), 3004–3016. https://doi.org/10.1021/acsnano.9b07866.

(17) Zak, A.; Sallacan-Ecker, L.; Margolin, A.; Feldman, Y.; Popovitz-Biro, R.; Albu-Yaron, A.; Genut, M.; Tenne, R. Scaling Up of the WS2 Nanotubes Synthesis. *Fullerenes, Nanotubes and Carbon Nanostructures* **2010**, *19* (1–2), 18–26. https://doi.org/10.1080/1536383X.2010.488594.

(18) Liu, Z.; Murphy, A. W. A.; Kuppe, C.; Hooper, D. C.; Valev, V. K.; Ilie, A. WS_2 Nanotubes, 2D Nanomeshes, and 2D In-Plane Films through One Single Chemical Vapor Deposition Route. *ACS Nano* **2019**, *13* (4), 3896–3909. https://doi.org/10.1021/acsnano.8b06515.

(19) Kundrát, V.; Novák, L.; Bukvišová, K.; Zálešák, J.; Kolíbalová, E.; Rosentsveig, R.; Sreedhara, M. B.; Shalom, H.; Yadgarov, L.; Zak, A.; Kolíbal, M.; Tenne, R. Mechanism of WS_2 Nanotube Formation Revealed by *in Situ* / *Ex Situ* Imaging. *ACS Nano* **2024**, *18* (19), 12284–12294. https://doi.org/10.1021/acsnano.4c01150.

(20) Seo, B.; Jeong, H. Y.; Hong, S. Y.; Zak, A.; Joo, S. H. Impact of a Conductive Oxide Core in Tungsten Sulfide-Based Nanostructures on the Hydrogen Evolution Reaction. *Chem. Commun.* **2015**, *51* (39), 8334–8337. https://doi.org/10.1039/C5CC02472B.

(21) Qin, L.-C. Electron Diffraction from Carbon Nanotubes. *Rep. Prog. Phys.* **2006**, *69* (10), 2761–2821. https://doi.org/10.1088/0034-4885/69/10/r02.

(22) Deniz, H.; Derbakova, A.; Qin, L.-C. A Systematic Procedure for Determining the Chiral Indices of Multi-Walled Carbon Nanotubes Using Electron Diffraction—Each and Every Shell. *Ultramicroscopy* **2010**, *111* (1), 66–72. https://doi.org/10.1016/j.ultramic.2010.09.010.

(23) Liu, Z.; Qin, L.-C. A Practical Approach to Determine the Handedness of Chiral Carbon Nanotubes by Electron Diffraction. *Chemical Physics Letters* **2005**, *405* (4–6), 265–269. https://doi.org/10.1016/j.cplett.2005.02.042.

(24) Chen, Y.; Shen, Z.; Xu, Z.; Hu, Y.; Xu, H.; Wang, S.; Guo, X.; Zhang, Y.; Peng, L.; Ding, F.; Liu, Z.; Zhang, J. Helicity-Dependent Single-Walled Carbon Nanotube Alignment on Graphite for Helical Angle and Handedness Recognition. *Nat Commun* **2013**, *4* (1). https://doi.org/10.1038/ncomms3205.

(25) Odom, T. W.; Huang, J.-L.; Kim, P.; Lieber, C. M. Atomic Structure and Electronic Properties of Single-Walled Carbon Nanotubes. *Nature* **1998**, *391* (6662), 62–64. https://doi.org/10.1038/34145.

(26) Shen, J.; Zhang, D.; Zhang, F.-H.; Gan, Y. AFM Tip-Sample Convolution Effects for Cylinder Protrusions. *Appl. Surf. Sci* **2017**, *422*, 482–491. https://doi.org/10.1016/j.apsusc.2017.06.053.

(27) Yao, F.; Yu, W.; Liu, C.; Su, Y.; You, Y.; Ma, H.; Qiao, R.; Wu, C.; Ma, C.; Gao, P.; Xiao, F.; Zhao, J.; Bai, X.; Sun, Z.; Maruyama, S.; Wang, F.; Zhang, J.; Liu, K. Complete Structural Characterization of Single Carbon Nanotubes by Rayleigh Scattering Circular Dichroism. *Nat. Nanotechnol.* **2021**, *16* (10), 1073–1078. https://doi.org/10.1038/s41565-021-00953-w.

(28) Robertson, A. W.; Warner, J. H. Atomic Resolution Imaging of Graphene by Transmission Electron Microscopy. *Nanoscale* **2013**, *5* (10), 4079. https://doi.org/10.1039/c3nr00934c.

(29) Liu, Z.; Suenaga, K.; Yoshida, H.; Sugai, T.; Shinohara, H.; Iijima, S. Determination of Optical Isomers for Left-Handed or Right-Handed Chiral Double-Wall Carbon Nanotubes. *Phys. Rev. Lett.* **2005**, *95* (18), 187406. https://doi.org/10.1103/PhysRevLett.95.187406.

(30) Yu, Y.; Zhao, Y.; Li, S.; Zhao, C.; Liu, W.; Wang, S.; Ding, F.; Zhang, J. Determine the Complete Configuration of Single-Walled Carbon Nanotubes by One Photograph of Transmission Electron Microscopy. *Adv. Sci* **2023**, *10* (15). https://doi.org/10.1002/advs.202206403.

(31) Chen, Y.; Deniz, H.; Qin, L.-C. Accurate Measurement of the Chirality of WS_2 Nanotubes. *Nanoscale* **2017**, *9* (21), 7124–7134. https://doi.org/10.1039/C7NR01688C.

(32) Deniz, H.; Qin, L.-C. Determination of the Chiral Indices of Tungsten Disulfide (WS2) Nanotubes by Electron Diffraction. *Chem. Phys. Lett* **2012**, *552*, 92–96. https://doi.org/10.1016/j.cplett.2012.09.041.

(33) Oster, G.; Nishijima, Y. MOIRÉ PATTERNS. *Scientific American* **1963**, *208* (5), 54–63.

(34) Sadan, M. B.; Houben, L.; Enyashin, A. N.; Seifert, G.; Tenne, R. Atom by Atom: HRTEM Insights into Inorganic Nanotubes and Fullerene-like Structures. *Proc. Natl. Acad. Sci. U.S.A.* **2008**, *105* (41), 15643–15648. https://doi.org/10.1073/pnas.0805407105.

(35) Sinha, S. S.; Yadgarov, L.; Aliev, S. B.; Feldman, Y.; Pinkas, I.; Chithaiah, P.; Ghosh, S.; Idelevich, A.; Zak, A.; Tenne, R. MoS_2 and WS_2 Nanotubes: Synthesis, Structural Elucidation, and Optical Characterization. *J. Phys. Chem. C* **2021**, *125* (11), 6324–6340. https://doi.org/10.1021/acs.jpcc.0c10784.

(36) Chithaiah, P.; Ghosh, S.; Idelevich, A.; Rovinsky, L.; Livneh, T.; Zak, A. Solving the "MoS_2 Nanotubes" Synthetic Enigma and Elucidating the Route for Their Catalyst-Free and Scalable Production. *ACS Nano* **2020**, *14* (3), 3004–3016. https://doi.org/10.1021/acsnano.9b07866.

(37) Nakanishi, Y.; Furusawa, S.; Sato, Y.; Tanaka, T.; Yomogida, Y.; Yanagi, K.; Zhang, W.; Nakajo, H.; Aoki, S.; Kato, T.; Suenaga, K.; Miyata, Y. Structural Diversity of Single-Walled Transition Metal Dichalcogenide Nanotubes Grown via Template Reaction. *Adv Mater* **2023**, *35* (46), 2306631. https://doi.org/10.1002/adma.202306631.

(38) Kanda, N.; Nakanishi, Y.; Liu, D.; Liu, Z.; Inoue, T.; Miyata, Y.; Tománek, D.; Shinohara, H. Efficient Growth and Characterization of One-Dimensional Transition Metal Tellurides inside Carbon Nanotubes. *Nanoscale* **2020**, *12* (33), 17185–17190. https://doi.org/10.1039/D0NR03129A.

(39) Çaha, I.; Ahmad, A. U.; Boddapatti, L.; Bañobre-López, M.; Costa, A. T.; Enyashin, A. N.; Li, W.; Gargiani, P.; Valvidares, M.; Fernández-Rossier, J.; Deepak, F. L. One-Dimensional CrI3 Encapsulated within Multi-Walled Carbon Nanotubes. *Commun Chem* **2025**, *8* (1), 155. https://doi.org/10.1038/s42004-025-01550-x.

Supplementary Information for

Quantifying chiral handedness of core-shell inorganic nanotube photocatalysts via electron microscopy and diffraction

Kaiyuan Wang,[a] *Beilynn Geiss,*[b] *Roy Geiss,*[c] *James R. Neilson,*[a] *Alla Zak,*[d] *Justin B. Sambur*[a]

[a]Department of Chemistry, Colorado State University, 200 West Lake Street, Fort Collins,
Colorado 80523-1872, United States.

[b]Skidmore College, Saratoga Springs, New York 12866, United States.

[c]Analytical Resources Core, Colorado State University, 200 West Lake Street, Fort Collins,
Colorado 80523-1872, United States.

[d] Faculty of Science, Holon Institute of Technology, Holon 5810201, Israel.

*Corresponding Author:

E-mail: Justin.Sambur@colostate.edu

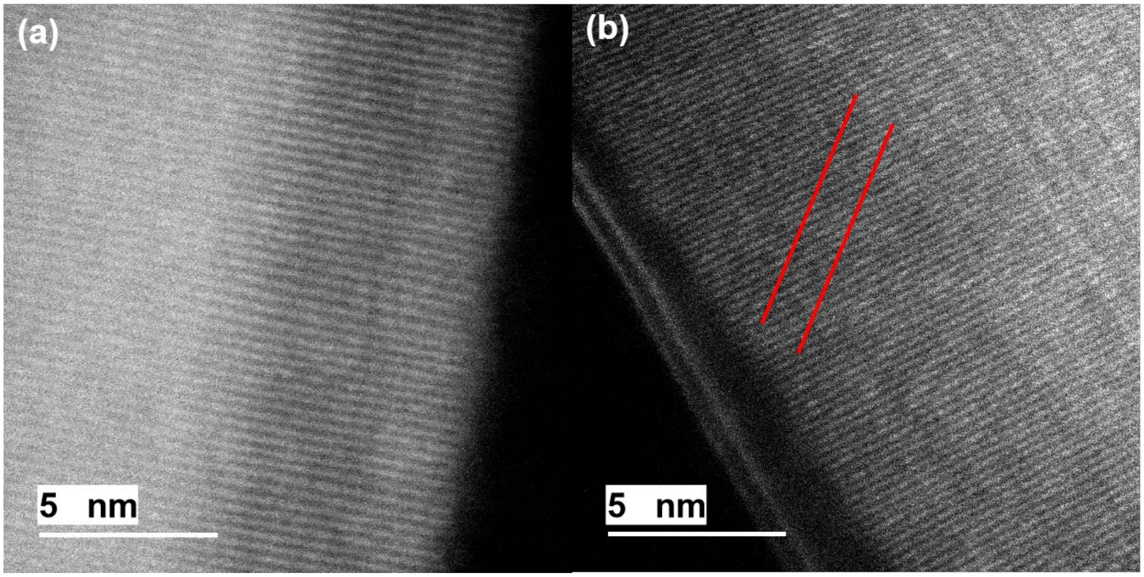

Figure S1. High-angle annular dark-field scanning transmission electron microscopy image of **(a)** a tungsten oxide rod without WS_2 layers, and **(b)** a multi-wall WS_2 NT with tungsten oxide core. The moiré patterns are indicated by red lines.

TEM Image Analysis Procedure.

FFT to IFFT image analysis approach. Figure S2 and Figure S6 illustrate the image analysis approach and the caption describes each step in the approach. First, a local region of an NT image(Figure S2a) is selected and transformed to reciprocal space by FFT (Figure S2b). In the FFT, the WS_2 lattice fringes appear as lines aligned along a direction that is perpendicular to the fringes seen in the TEM image. Next, the user can define a region of interest in the FFT image using the mask function in the Digital Micrograph software to select the band of reciprocal space frequencies that lie along the WS_2-related direction in the FFT (white regions in Figure S2c). The circled spots in Figure S2b simply mark the WS_2-related direction; they are not the complete set of WS_2 frequencies. The mask retains the whole directional frequency band, since only the orientation is required for visualization. Lastly, applying the IFFT to the masked FFT to reconstruct a real-space image in which the WS_2 lattice orientation is clearly enhanced (Figure S2d).

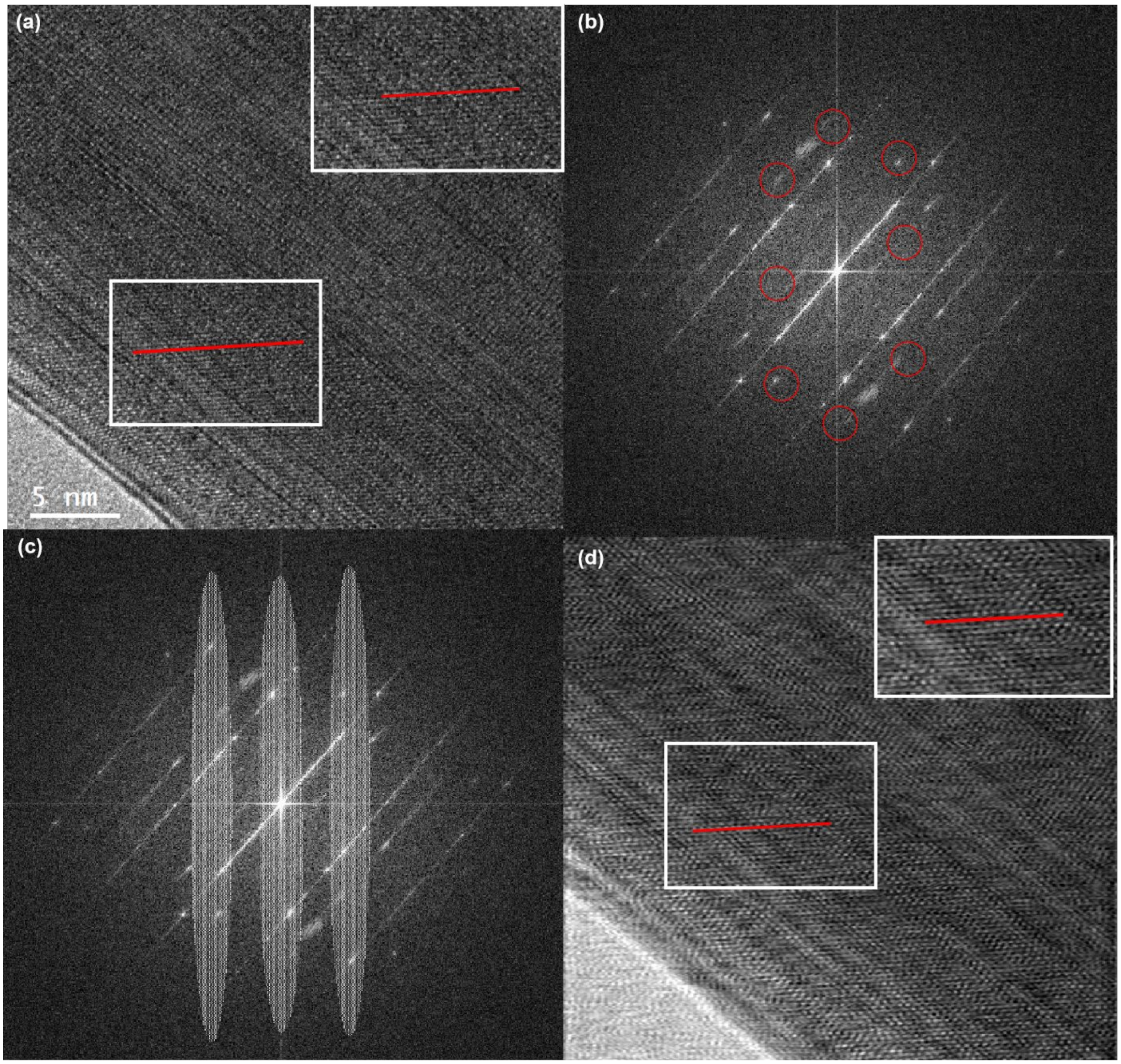

Figure S2. Identifying the WS_2 lattice fringes in TEM using Fast Fourier Transform (FFT) and Inverse Fast Fourier Transform (IFFT). **(a)** Selected area of the TEM image from Figure 5a in the main text. The inset shows a zoomed-in view of the WS_2 lattice (red line) indicated by the white box. **(b)** FFT image of panel (a), where the red circles indicate the WS_2-related FFT spots. **(c)** A user-defined region of interest (white regions), or mask, is placed on the FFT image perpendicular to the lattice fringes in real space. **(d)** IFFT reconstructed image from the regions of interest in panel (c). The inset shows a zoomed-in view of the WS_2 lattice (red line) indicated by the white box.

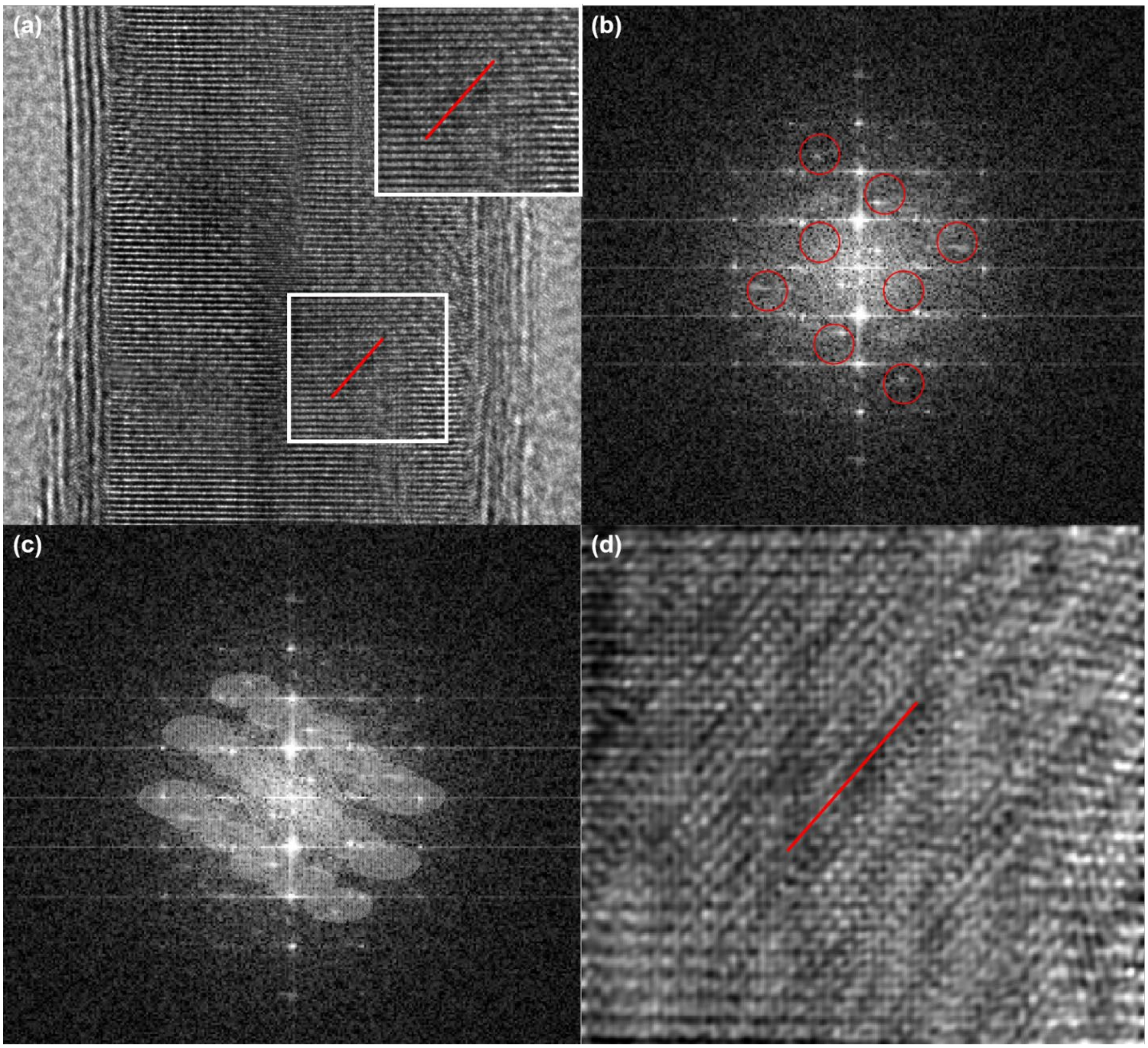

Figure S3 Identifying the WS_2 lattice in TEM using Fast Fourier Transform (FFT) and Inverse Fast Fourier Transform (IFFT). **(a)** Selected area of the TEM image from Figure 5b in the main text. The inset shows a zoomed-in view of the WS_2 lattice (red line) indicated by the white box. **(b)** The FFT image, where the red circles indicate the WS_2-related direction suggested in (a). **(c)** Mask and keep the area (white region) corresponding to the WS_2-related direction, which is perpendicular to the lattice fringes in real space. **(d)** The IFFT reconstructed image shows a the WS_2 lattice (red line).

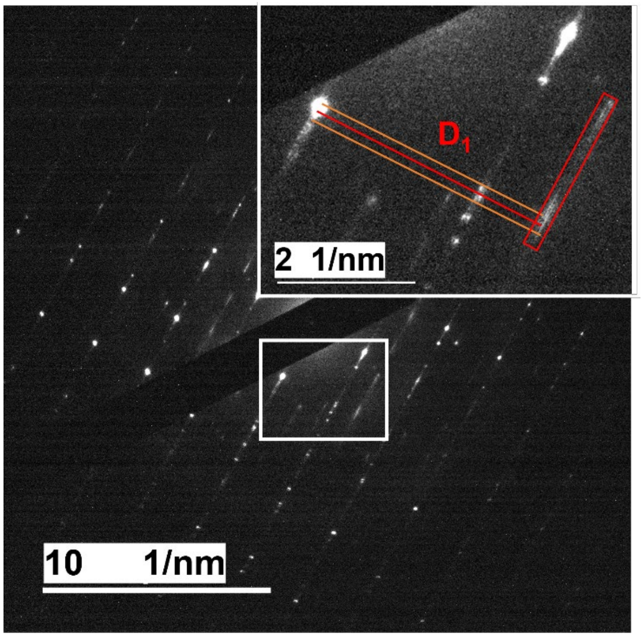

Figure S4. Measurement of the d-spacing in the SAED pattern. The d-spacing is defined as the distance between a diffraction line and the equatorial line. The inset shows a magnified view of the boxed region: orange lines mark the longest and shortest measured distances, and the red line indicates the averaged distance used in this work. The red box highlights the treatment of diffraction from multiple WS_2 shells as a single line.

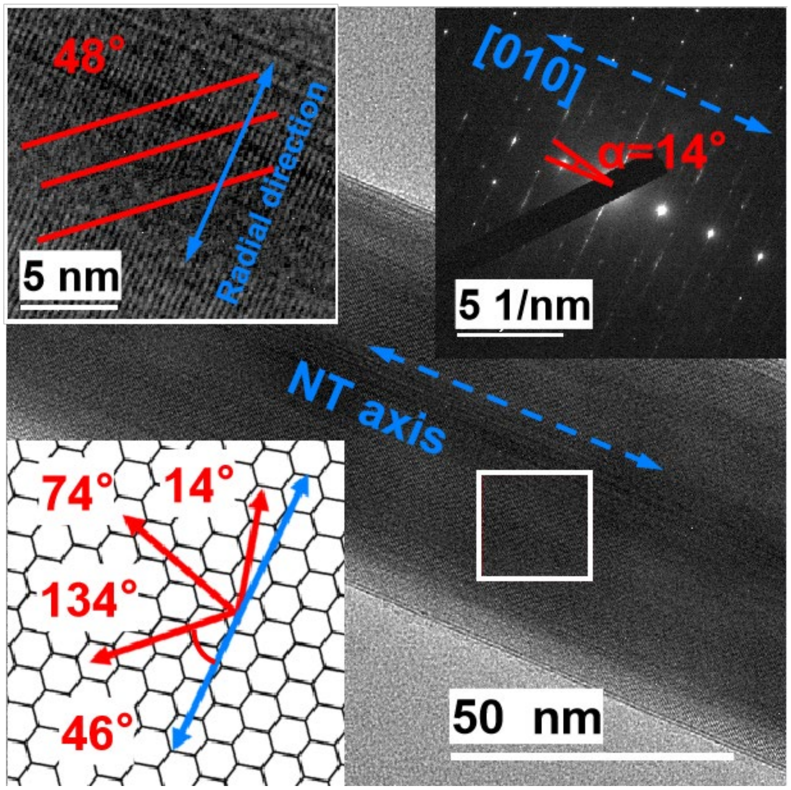

Figure S5. Another example of handedness identification. Insets (top-left) are a zoom-in view of the boxed TEM region, highlighting the 48° chiral angles (red) and (top-right) 14° chiral angles measured in its SAED pattern. The bottom left inset shows the reference frame that relates the TEM-derived angle in the lower right inset (48°) to the chiral angle measured via SAED.

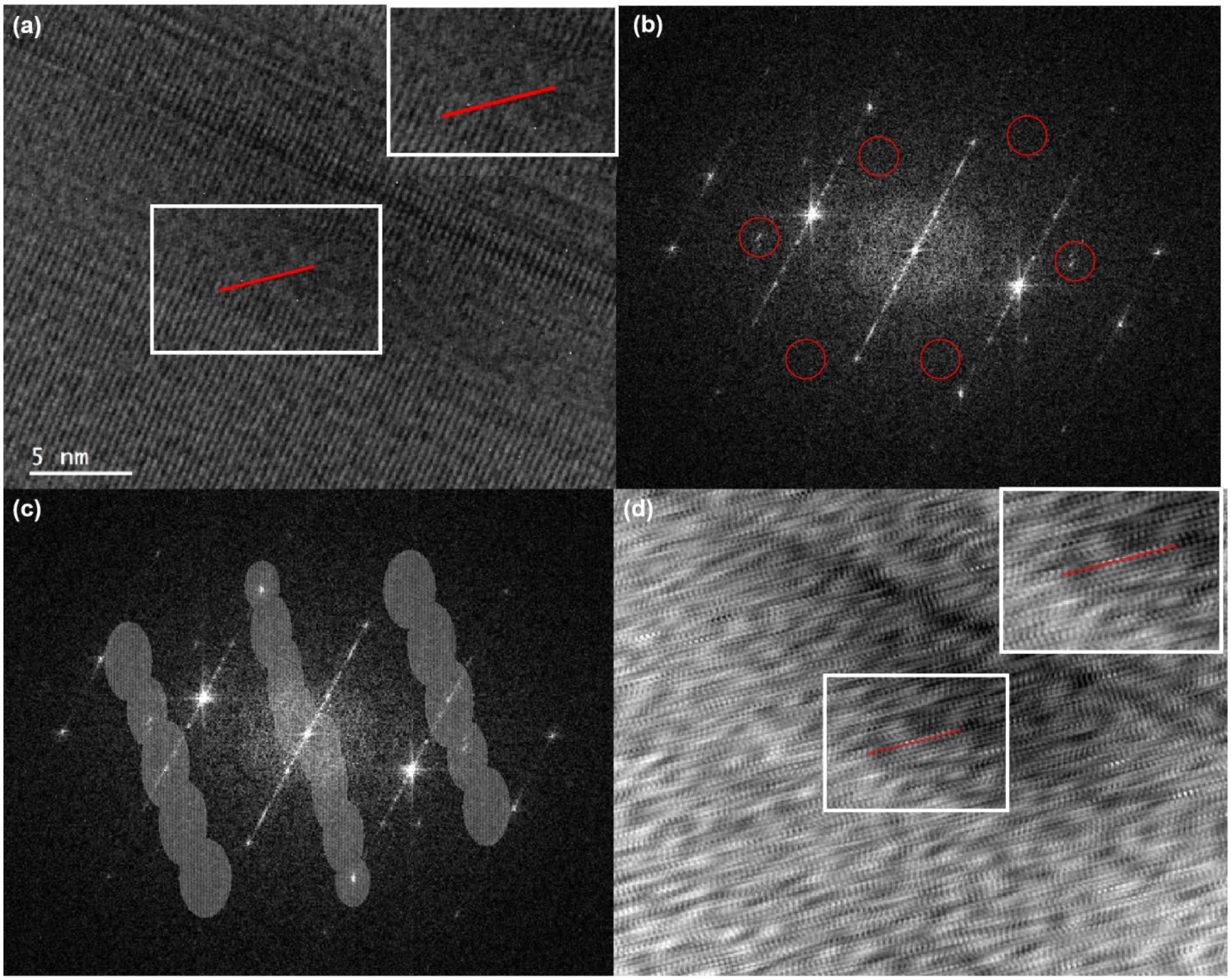

Figure S6. Identifying the WS_2 lattice in TEM using Fast Fourier Transform (FFT) and Inverse Fast Fourier Transform (IFFT). (a) Selected area of the TEM image from Figure S5. The inset shows a zoomed-in view of the WS_2 lattice (red line) indicated by the white box. (b) The FFT image, where the red circles indicate the WS_2-related direction suggested in (a). (c) Mask and keep the area (white region) corresponding to the WS_2-related direction, which is perpendicular to the lattice fringes in real space. (d) IFFT reconstructed image. The inset shows a zoomed-in view of the WS_2 lattice (red line) indicated by the white box.

Qualitative approach. Alternatively, lattice fringes may appear in TEM images as shown in Figure 3. Three main steps were used to qualitatively identify WS_2 lattice fringes in TEM images. First, we obtained TEM images and SAED patterns of a single NT. The chiral angle can be derived from the SAED pattern by measuring the D-spacings. The midpoint of the diffraction line should be taken as the endpoint (Figure S4) to generate an average value of all possible layers within a multiwalled NT. Two D-spacings (D_1 and D_2, or D_1 and D_3, or D_2 and D_3) are sufficient for calculating the chiral angle, and the relevant equations are provided in the main text.

Second, we identify the WS_2 lattice line in the TEM image that corresponds to the chiral angle measured from the SAED pattern. In some cases, this WS_2 line can be directly observed without a moiré pattern, while in other cases, the moiré pattern is observed (Figure 6). In such cases, the moiré pattern can serve as a guide: the WS_2 lattice lines run in the opposite direction to the moiré pattern. Consistency between the SAED-derived angle and the TEM image further verifies whether the observed lines correspond to the WS_2 lattice or to the moiré pattern, as shown in the reference frames in main text figures. Practical adjustments such as zooming in or out and slowly moving the figure can help to distinguish between the two.

Third, we determine the handedness based on the angle measured in the TEM image. If the angle is between 0° and 30°, the handedness follows the oriented direction of the lattice lines. For instance, a 15° left orientation indicates a left-handed NT. If the angle is between 30° and 60°, the handedness is opposite to the orientation direction (Figure 6). For example, a 45° left orientation indicates a right-handed NT.

An optional fourth step is to perform a simulation to further validate the assignment. Using the structure and parameters measured in TEM images, one can simulate the moiré pattern by overlapping the strip-like tungsten oxide and the hexagonal WS_2 lattice (Figure 6). This simulated pattern can then be directly compared with the experimental TEM images to check consistency.

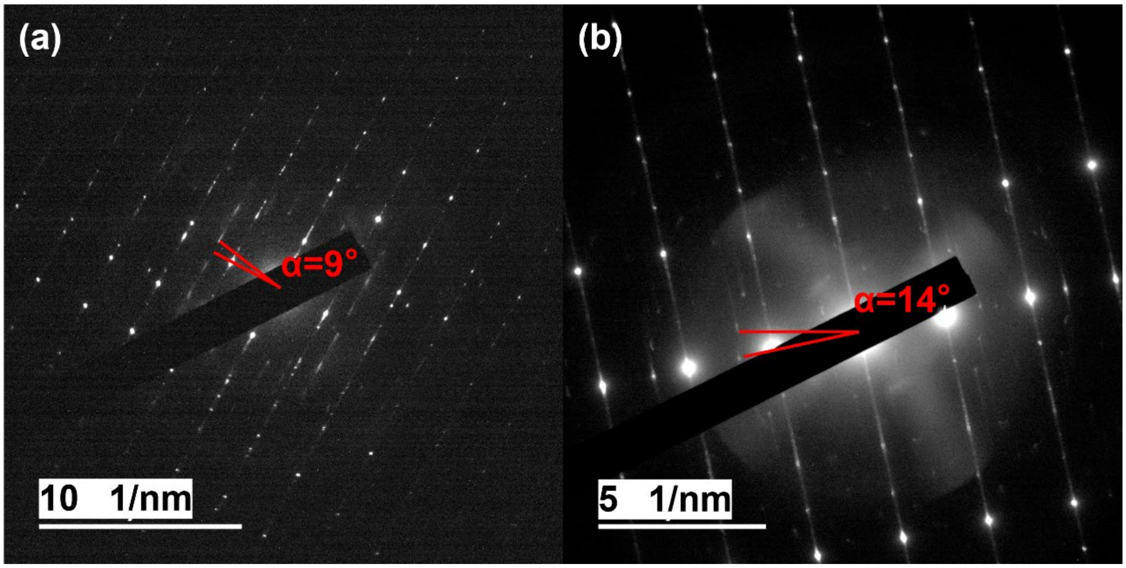

Figure S7. Chiral angles measured from the SAED patterns of **(a)** the WS_2 NT shown in Figure 6a and **(b)** the NT shown in Figure S5. The number of diffraction lines corresponds to the number of WS_2 shells, with each shell contributing a slightly different chiral angle (typically differing by a few degrees). In this work, such minor inter-shell angular variations are neglected. Instead, the diffraction pattern is treated as a single effective line, and the average chiral angle is determined by measuring the distance between the equatorial line and the midpoint of the diffraction line.

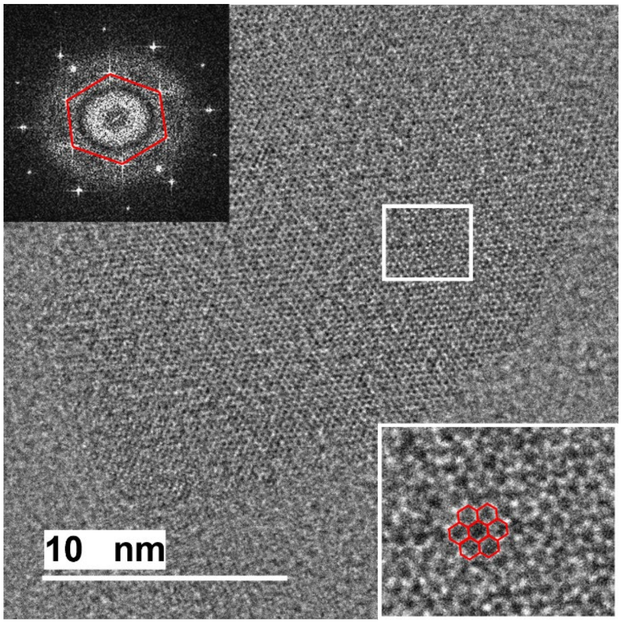

Figure S8. TEM image of a peeled-off WS_2 layer viewed along the [001] zone axis. Insets: (bottom right) a magnified view of the boxed region; (top left) the Fast Fourier Transform (FFT) calculated from a larger region of the same layer. The red marks highlight the hexagonal lattice.